THE EFFECT OF FRACTAL ORIFICES ON THE ENTRAINMENT OF SYNTHETIC JETS

Congyi Xu
Fluid Mechanics Key Laboratory of Education Ministry
Beihang University
Beijing, China
xucongyi@buaa.edu.cn

Jinjun Wang
Fluid Mechanics Key Laboratory of Education Ministry
Beihang University
Beijing, China
jjwang@buaa.edu.cn

ABSTRACT

The effect of fractal orifices on the entrainment of synthetic jets is investigated. Synthetic jets with circular and fractal orifices, as well as a continuous jet with a circular orifice at $Re_j = 3150$, are measured using two-dimensional particle image velocimetry. The results of the half-width and entrainment coefficient show that the entrainment performance of the fractal synthetic jet is lower than that of the circular synthetic jet. To explore the mechanism of the influence of fractal orifice on entrainment, the turbulent/non-turbulent interface (TNTI) properties of the synthetic jets are analysed. The result indicates that the fractal orifice reduces the TNTI tortuosity, leading to the reduction of the area where the entrainment process occurs. Additionally, the fractal orifice weakens the vortex near TNTI, leading to a decrease in the enstrophy production. These modifications of the TNTI result in that the lower entrainment performance of the fractal synthetic jet.

INTRODUCTION

Synthetic jets (Smith & Glezer, 1998) are active flow control techniques developed over the past two decades. Due to their advantages of no external air source, simple actuator structure and enhanced entrainment characteristics, synthetic jets have been applied in flow control fields such as fluid mixing, suppression of flow separation, and enhancement of heat transfer.

The behaviour of synthetic jets has been extensively studied through experimental and numerical methods, and the insights into the entrainment mechanism of synthetic jets have been proposed. Earlier studies (Cater & Soria, 2002; Smith & Swift, 2003; Krishnan & Mohseni, 2009) have generally attributed the enhanced entrainment of synthetic jets to the effect of vortex rings or strong velocity fluctuations in the near field. However, recent studies (Xia & Mohseni, 2018; Xu et al., 2023) have found that enhanced entrainment of synthetic jets occurs in the transition region between the near field dominated by vortex rings and the far field where the flow is fully developed. Xu et al. (2023) found in their experimental studies on synthetic and continuous jets that the spreading rate, centre-line velocity decay, and the growth rate of mean turbulent/non-turbulent interface radial position all increase after the vortex rings breakdown. They suggested that the "breakdown of the vortex ring", instead of the vortex ring, enhances the entrainment in the synthetic jet.

The influence of non-circular orifice shapes, such as rectangles and ellipses, on the entrainment of synthetic jets has been studied (Wang et al., 2018; Shi et al., 2019), but research on synthetic jets with fractal orifices is still lacking. According to the research on continuous jets with fractal orifice (Breda & Buxton, 2018), the fractal orifice suppresses the large-scale coherent structures in the near field, leading to a decrease in the entrainment coefficient. The aim of this paper is to study the effect of fractal orifices on the vortex ring of synthetic jets and its subsequent breakdown on the entrainment process.

EXPERIMENTAL METHODS

A brief description of the continuous jet nozzle and synthetic jet actuator is provided here, and detailed information about the device can be found in the previous work (Xu et al., 2023). The seeded air, controlled by the flow controller, forms a stable continuous jet after passing through the honeycomb, screen and contraction section of the continuous jet nozzle. Synthetic jets are generated by an actuator based on a piezoelectric ceramic diaphragm. A sinusoidal signal is generated by the Tektronix AFG1062 signal generator, and amplified by the Aigtek ATA-214 voltage amplifier, and then applied to the piezoelectric ceramic diaphragm to generate a synthetic jet at the orifice. As shown in figure 1, the orifice shapes are circular and Koch snowflake fractal with 2 and 3 iterations, respectively. The longer and shorter axes of symmetry of the fractal orifices are referred to as the major axis and minor axis, respectively. The circular orifice diameter D and the equivalent diameter $D_e = \sqrt{4S/\pi}$ of the fractal orifice are both 5 mm, where S is the orifice area. Both of the above diameters are denoted by D hereafter. The synthetic jets with circular orifice and fractal orifices are studied at jet Reynolds number $Re_j = 3150$, and the continuous jet at the same jet Reynolds number with circular orifice is taken as a contrast. The flow at the orifice of the
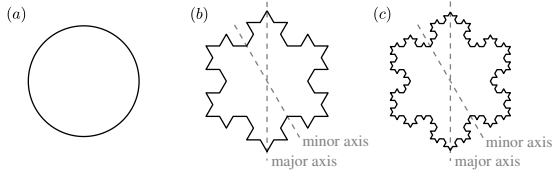
Figure 1. Jet orifices. (a) Circular orifice, (b) Koch snowflake fractal orifice with 2 iterations, and (c) Koch snowflake fractal orifice with 3 iterations.
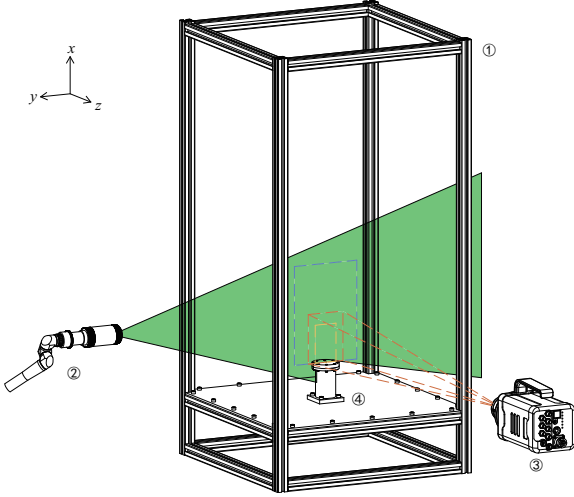

Figure 2. Schematic of the (1) container, (2) laser head connected to a light arm, (3) high-speed camera, and (4) jet generator (continuous jet nozzle or synthetic jet actuator).

Figure 3. Variations of jet half-width $r_{1/2}$. In the legend, 'CJ' and 'SJ' represent the continuous jet and synthetic jet, respectively. The 'round', 'koch2', and 'koch3' represent the circular orifice, Koch snowflake fractal orifice with 2 and 3 iterations, respectively.

synthetic jet actuators is measured by the HangHua CTA-02A hot-wire anemometer to obtain the frequency and voltage characteristics. In the present experiment, the driving frequency f_d of the piezoelectric ceramic diaphragm is fixed at the resonance frequency of 500 Hz, and the time-averaged blowing velocity U_0 at the orifice is adjusted by changing the driving voltage.

Time-resolved two-dimensional particle image velocimetry (TR-2DPIV) experiments are conducted in a container with size of 0.5 m × 0.5 m × 1 m. The coordinate system is defined in figure 2, and the centre of the orifice is taken as the origin. A laser sheet produced by the Beamtech Vlite-Hi-527 Nd:YAG dual-cavity laser illuminates the x-y plane through the jet centreline. The particle images are captured by the Photron Nova R2 high-speed camera with a Nikon 50 mm lens and processed by the multi-pass iterative Lucas–Kanade algorithm (Champagnat et $al.$, 2011; Pan et $al.$, 2015) to obtain the velocity field. For each jet, the experiments are performed in three fields of view, detailed in table 1. For the synthetic jets with fractal orifices, measurements are conducted in both the major and minor planes, but the results obtained from the two planes show minimal discrepancies. Therefore, only the results from the major plane are presented in the subsequent sections.

RESULTS
Jet Entrainment Characteristics

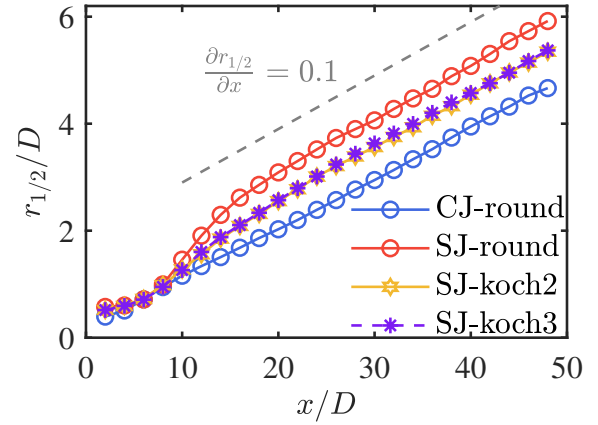Statistics of jets are presented in this section to compare the differences in entrainment characteristics between the studied jets.

The variations of jet half-width $r_{1/2}$ are shown in figure 3. The growth rates of half-width $\partial r_{1/2}/\partial x$, i.e. the spreading rates, of all jets in the far field are close to the value 0.1 reported in the previous studies (Cater & Soria, 2002; Mistry et $al.$, 2016). The spreading rate of the circular synthetic jet is significantly higher than that of the continuous jet at approximately $10 < x/D < 20$, while the spreading rate of the fractal synthetic jets are between the two jets. The result indicates that fractal orifices decrease the entrainment of synthetic jets, although it remains greater than that of the continuous jet. In addition, the results obtained for the two fractal synthetic jets, both in the current analysis and subsequent analyses, are nearly identical. This similarity mainly arises because the side length of the fractal orifice for SJ-koch3 case (approximately 0.2 mm) is already equivalent to the Kolmogorov scale, thereby not significantly affecting the flow field.

Entrainment coefficient, denoted by α, quantifies entrainment of environmental fluid into the turbulent flow, and is used to describe the local entrainment of a jet. Detailed definition and calculation process of entrainment coefficient can be found in the previous studies (Breda & Buxton, 2018; Xu et $al.$, 2023). Figure 4 shows the variations of the entrainment coefficient α of the jets. The entrainment coefficients of all jets in the far field remain stable around the constant value of 0.08 observed in fully developed jets (van Reeuwijk & Craske, 2015). The entrainment coefficient of the circular synthetic jet exhibits a peak value at approximately $x/D = 10$, which is the most obvious part of the enhanced entrainment of the synthetic jet compared with the continuous jet. The enhanced entrainment here is due to the enhanced vortex near the TNTI caused by the vortex ring breakdown (Xu & Wang, 2024). However, in the fractal synthetic jets, the peak almost disappears, and the entrainment coefficient has stabilised at approximately 0.08 after $x/D = 10$. The results suggest that the fractal orifices modify the near-field flow structure of the synthetic jets. Next, the evolution of the flow structure in the synthetic jets will be analysed.

Table 1.   PIV experiment details.

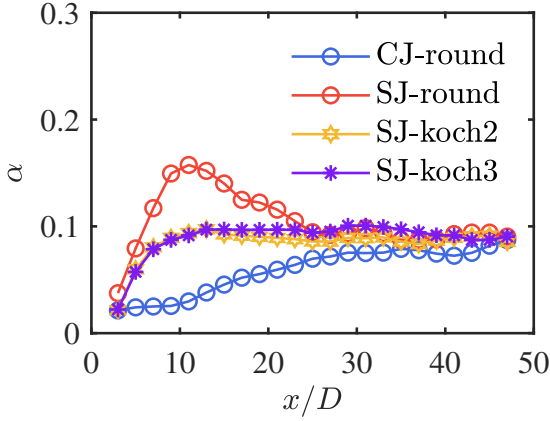| Experiment details	FOV1(yellow)	FOV2(red)	FOV3(blue)
Range of FOV	$0 < x/D < 20$	$0 < x/D < 26$	$0 < x/D < 52$
Image size	1024×672	1792×1408	2048×1472
Interrogation window	32×32	32×32	32×32
Overlap	75%	75%	75%
Sampling frequency (Hz)	3000	1000	500
Number of realizations	30000	7500	7500

Figure 4.   Variations of entrainment coefficient α.

Flow Structure Evolution

The formation, convection and breakdown of vortex rings are typical evolution processes in the near field of synthetic jets. The criterion λ_{ci}, denoting the local swirling strength of the vortex, is utilized to identify vortices for visually examining the evolution processes of vortex rings (Zhou *et al.*, 1999). The phase-averaged $\lambda_{ci}D/U_0$ field of the SJ-koch2 case is shown in figure 5. Given the similarity between the SJ-koch2 and SJ-koch3 case, the phase-averaged $\lambda_{ci}D/U_0$ field for the latter is omitted here for brevity. The result shows that the fractal orifice does not prevent the formation of vortex rings, and the evolution process of the vortex rings in the fractal synthetic jet shown in figure 5 is qualitatively similar to that of the previous circular synthetic jet (Xu & Wang, 2024).

Fourier mode decomposition (FMD) (Ma *et al.*, 2015) is applied to the flow field in order to quantitatively determine the breakdown position of the vortex ring in the fractal synthetic jets. This method decomposes the flow field data containing multifrequency information into a series of modes according to the characteristic frequency, with each mode corresponding to a specific frequency coherent structure. Applying the Fourier transform to each grid point in space extends the single-point Fourier transform to the entire flow field, yielding a matrix

$$\mathbf{c_k} = \frac{1}{N}\sum_{n=0}^{N-1} \mathbf{F_n} e^{-i\frac{2\pi k}{N}n} \tag{1}$$

that contains the spectral information of the entire flow field. Matrix $\mathbf{c_k}$ is referred to as the dynamic mode or the Fourier
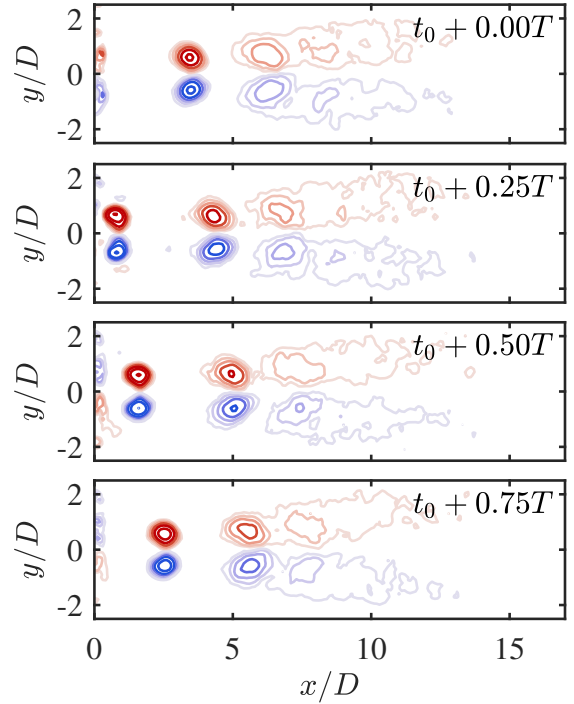

Figure 5.   Phase-averaged $\lambda_{ci}D/U_0$ field of the SJ-koch2 case over a period. Here λ_{ci} is normalised by the orifice diameter D and the time-averaged blowing velocity U_0. The sign of λ_{ci} is identical to the local vorticity.

mode. The amplitudes of the Fourier mode based on the radial fluctuation velocity v' at the characteristic frequency of $f/f_d = 1$ along the lines around the edge of the orifice (i.e. $y/D = 0.5$) are plotted in figure 6. The higher Fourier mode amplitude in the region near the orifice indicates dominance by the vortex ring. As the jet develops, the vortex ring is broken and loses its periodicity, leading to a reduction in the Fourier mode amplitude corresponding to the driving frequency. The position where the slope of the Fourier mode amplitude curve changes abruptly can be considered as the position of the vortex ring breakdown, which corresponds to the intersection of the fitted lines in figure 6. The results indicate that although the Fourier mode amplitude of the fractal synthetic jet is slightly lower than that of the circular synthetic jet near the vortex ring breakdown position, the vortex ring breakdown position of the fractal synthetic jet does not change significantly com-
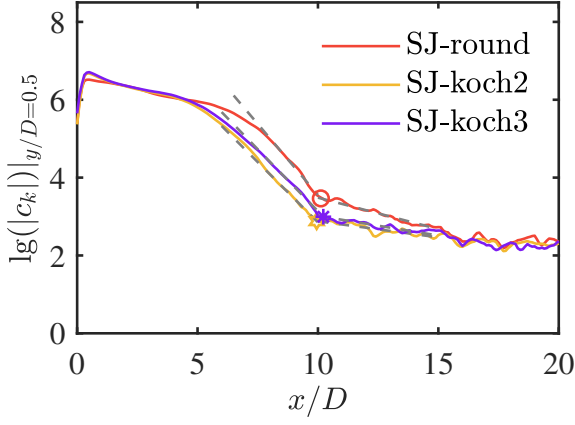
Figure 6. Amplitude of the Fourier mode at the characteristic frequency of $f/f_d = 1$ along the line $y/D = 0.5$, based on the radial fluctuation velocity v'. The dashed lines and markers represent the fitting lines and the intersection points of the fitting lines, respectively.

Figure 7. Instantaneous enstrophy fields of the circular synthetic jet in logarithmic scaling. The TNTI is denoted by the black solid line.

pared with that of the circular synthetic jet. This observation is consistent with the qualitative results of the phase-averaged $\lambda_{ci}D/U_0$ field and the variation of jet half-width described above.

Turbulent/non-turbulent Interface

The turbulent/non-turbulent interface (TNTI) (da Silva *et al.*, 2014) is a very thin layer of fluid that separates turbulent and non-turbulent regions in the instantaneous flow. Entrainment can be characterized by the transport of non-turbulent fluid across the TNTI. In the present study, spanwise vorticity magnitude $|\omega_z|$ is used as an indicator scalar to identify TNTI (Balamurugan *et al.*, 2020; Xu *et al.*, 2023). The suitable thresholds for the four cases are determined using an empirical process based on evaluating the area-averaged values. For a given variable f, a conditional average function is introduced as

$$\widetilde{f}(|\omega_z|_{th}) = \frac{\int (f\, da)|_{|\omega_z| > |\omega_z|_{th}}}{\int da|_{|\omega_z| > |\omega_z|_{th}}}. \quad (2)$$

The inflection point of the conditional average function is used as a threshold to detect TNTI in the previous studies (Mistry *et al.*, 2016; Kohan & Gaskin, 2022). Following this method, the TNTIs for the four cases are identified, and figure 7 illustrates the TNTI in the circular synthetic jet.

The geometry of the TNTI is highly distorted, and in order to quantify this property, the tortuosity is defined as the length of TNTI per streamwise distance L_i/L_x in two dimensions. The calculation of tortuosity is carried out using a sliding window with a width of $2D$, and varying the window width from $1D$ to $3D$ does not affect the conclusion. Greater tortuosity indicates that the TNTI has a larger surface area within the same streamwise distance. This condition is conducive to the fluid entering the turbulent region through the nibbling process, thereby enhancing the entrainment characteristics of the jet. Figure 8 illustrates the variations of the TNTI tortuosity of the synthetic jets. The TNTI tortuosity decreases slightly in the near field, which is related to the fact that the large-scale coherent structure increases the two-dimensionality of the flow (Xu
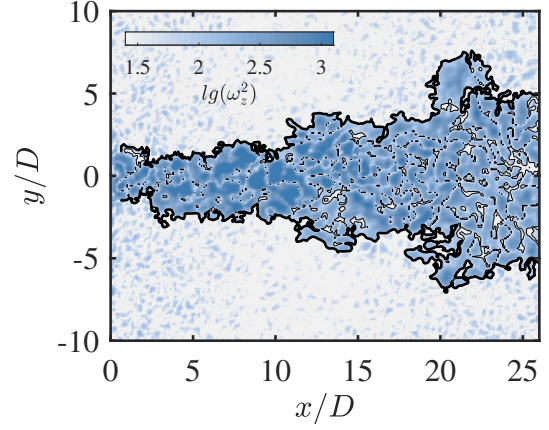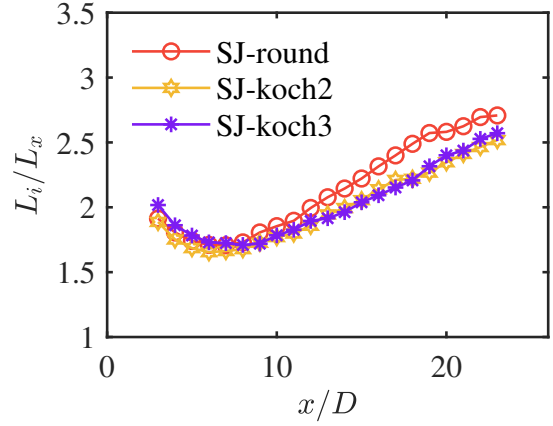

Figure 8. Variations of TNTI tortuosity L_i/L_x.

et al., 2023). After approximately $x/D = 10$, the growth rates of the TNTI tortuosity of the fractal synthetic jets are smaller than that of the circular synthetic jet, leading to the decline of its entrainment performance.

In addition to the geometric properties of the TNTI, the vortex dynamics near the TNTI have been proved to have an important effect on the entrainment process. The vortex near the TNTI will induce a compressive strain normal to the TNTI and an extensive strain parallel to the TNTI (Watanabe *et al.*, 2014; Mistry *et al.*, 2019). The alignment of the extensive strain and the vorticity vector results in a larger enstrophy production, allowing more environment irrotational fluid to gain vorticity, thereby enhancing local entrainment. Here, the vorticity at the centre of the vortices near the TNTI is measured to quantify their strength. Only those vortices whose centres are less than 15η away from the TNTI are included in the statistics, where η represents the local Kolmogorov scale. The value of 15η is chosen as the thickness of TNTI based on the previous studies (Zecchetto & da Silva, 2021; Xu *et al.*, 2023). Figure 9 illustrates the variations of vorticity at the centres of vortices near the TNTI. For all three synthetic jets, the vortex strength near the TNTI reaches its peak at the vortex breakdown position. This reflects that the transfer of turbulent kinetic energy from the coherent large-scale structure to
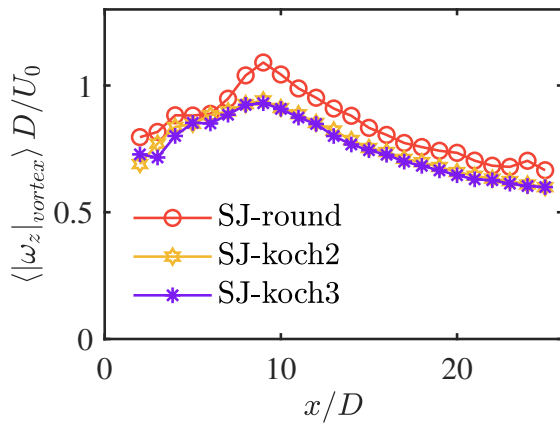
Figure 9. Variations of vorticity at the centres of vortices near TNTI. The conditional average of the vortices over all snapshots is denoted by $\langle \cdot \rangle$.

the random small-scale structure, enhancing the vortices near the TNTI. The smaller peak value of the fractal synthetic jets implies that the fractal orifices suppress the above transfer process, leading to the reduction of entrainment.

CONCLUSION

In this paper, synthetic jets with circular and fractal orifices, as well as a continuous jet with a circular orifice at $Re_j = 3150$, are measured using two-dimensional particle image velocimetry.

The analysis of jet half-width and entrainment coefficient shows that the fractal orifices mainly affect the transition region between the near field dominated by the vortex ring of the synthetic jets and the far field where the jet is fully developed. In this region, the entrainment performance of the fractal synthetic jets is lower than that of the circular synthetic jet, but still higher than that of the continuous jet.

The flow structure evolution of the synthetic jets is examined using the criterion λ_{ci} and Fourier mode decomposition. The results indicate that the fractal orifice does not change the breakdown position of the vortex ring but does cause a slight weakening in the strength of the vortex ring.

The empirical method based on conditional average function is used to determine the appropriate vorticity magnitude threshold and identify the TNTI. For the geometric properties, the fractal orifice reduces the TNTI tortuosity after the synthetic jet vortex ring is broken, resulting in a reduction of the entrainment area. For the dynamic properties, the fractal orifice weakens the vortex near the TNTI, leading to a decrease in the enstrophy production. All the above results indicate that the fractal orifices modify the TNTI characteristics in the synthetic jet, thus reducing its entrainment.

REFERENCES

Balamurugan, G., Rodda, A., Philip, J. & Mandal, A. C. 2020 Characteristics of the turbulent non-turbulent interface in a spatially evolving turbulent mixing layer. *Journal of Fluid Mechanics* **894**, A4.

Breda, M. & Buxton, O. R. H. 2018 Influence of coherent structures on the evolution of an axisymmetric turbulent jet. *Physics of Fluids* **30** (3), 035109.

Cater, J. E. & Soria, J. 2002 The evolution of round zero-net-mass-flux jets. *Journal of Fluid Mechanics* **472**, 167–200.

Champagnat, F., Plyer, A., Le Besnerais, G., Leclaire, B., Davoust, S. & Le Sant, Y. 2011 Fast and accurate piv computation using highly parallel iterative correlation maximization. *Experiments in Fluids* **50** (4), 1169–1182.

Kohan, Khashayar F. & Gaskin, Susan J. 2022 On the scalar turbulent/turbulent interface of axisymmetric jets. *Journal of Fluid Mechanics* **950**, A32.

Krishnan, G. & Mohseni, K. 2009 Axisymmetric synthetic jets: An experimental and theoretical examination. *AIAA Journal* **47** (10), 2273–2283.

Ma, L. Q., Feng, L. H., Pan, C., Gao, Q. & Wang, J. J. 2015 Fourier mode decomposition of piv data. *Science China Technological Sciences* **58** (11), 1935–1948.

Mistry, D., Philip, J. & Dawson, J. R. 2019 Kinematics of local entrainment and detrainment in a turbulent jet. *Journal of Fluid Mechanics* **871**, 896–924.

Mistry, D., Philip, J., Dawson, J. R. & Marusic, I. 2016 Entrainment at multi-scales across the turbulent/non-turbulent interface in an axisymmetric jet. *Journal of Fluid Mechanics* **802**, 690–725.

Pan, C., Xue, D., Xu, Y., Wang, J. J. & Wei, R. J. 2015 Evaluating the accuracy performance of lucas-kanade algorithm in the circumstance of piv application. *Science China-Physics Mechanics & Astronomy* **58** (10), 104704.

van Reeuwijk, M. & Craske, J. 2015 Energy-consistent entrainment relations for jets and plumes. *Journal of Fluid Mechanics* **782**, 333–355.

Shi, X. D., Feng, L. H. & Wang, J. J. 2019 Evolution of elliptic synthetic jets at low reynolds number. *Journal of Fluid Mechanics* **868**, 66–96.

da Silva, Carlos B., Hunt, Julian C. R., Eames, Ian & Westerweel, Jerry 2014 Interfacial layers between regions of different turbulence intensity. *Annual Review of Fluid Mechanics* **46** (1), 567–590.

Smith, B. L. & Glezer, A. 1998 The formation and evolution of synthetic jets. *Physics of Fluids* **10** (9), 2281–2297.

Smith, B. L. & Swift, G. W. 2003 A comparison between synthetic jets and continuous jets. *Experiments in Fluids* **34** (4), 467–472.

Wang, L., Feng, L. H., Wang, J. J. & Li, T. 2018 Evolution of low-aspect-ratio rectangular synthetic jets in a quiescent environment. *Experiments in Fluids* **59** (6), 91.

Watanabe, T., Sakai, Y., Nagata, K., Ito, Y. & Hayase, T. 2014 Vortex stretching and compression near the turbulent/non-turbulent interface in a planar jet. *Journal of Fluid Mechanics* **758**, 754–785.

Xia, X. & Mohseni, K. 2018 Transitional region of a round synthetic jet. *Physical Review Fluids* **3** (1), 011901.

Xu, C. Y., Long, Y. G. & Wang, J. J. 2023 Entrainment mechanism of turbulent synthetic jet flow. *Journal of Fluid Mechanics* **958**, A31.

Xu, C. Y. & Wang, J. J. 2024 Vortex ring breakdown dominating the entrainment of a synthetic jet. *Journal of Fluid Mechanics* **980**, A5.

Zecchetto, M. & da Silva, C. B. 2021 Universality of small-scale motions within the turbulent/non-turbulent interface layer. *Journal of Fluid Mechanics* **916**, A9.

Zhou, J., Adrian, R. J., Balachandar, S. & Kendall, T. M. 1999 Mechanisms for generating coherent packets of hairpin vortices in channel flow. *Journal of Fluid Mechanics* **387**, 353–396.